Nanolaminates: Increasing Dielectric Breakdown Strength of Composites

Scott P. Fillery,[†,‡] Hilmar Koerner,[§] Lawrence Drummy,[§] Erik Dunkerley,[⊥] Michael F. Durstock,[‡] Daniel F. Schmidt,[⊥] and Richard A. Vaia*,[‡]

[†]National Research Council, Washington, DC, United States

[‡]Materials and Manufacturing Directorate, Air Force Research Laboratory, Wright Patterson Air Force Base, Ohio, United States

[§]UES, Dayton, Ohio, United States

[⊥]Department of Plastics Engineering, University of Massachusetts, Lowell, Lowell, Massachusetts, United States

Ⓢ *Supporting Information*

ABSTRACT: Processable, low-cost, high-performance hybrid dielectrics are enablers for a vast array of green technologies, including high-temperature electrical insulation and pulsed power capacitors for all-electric transportation vehicles. Maximizing the dielectric breakdown field (E_{BD}), in conjunction with minimization of leakage current, directly impacts system performance because of the field's quadratic relationship with electrostatic energy storage density. On the basis of the extreme internal interfacial area and ultrafine morphology, polymer-inorganic nanocomposites (PNCs) have demonstrated modest increases in E_{BD} at very low inorganic loadings, but because of insufficient control of the hierarchal morphology of the blend, have yielded a precipitous decline in E_{BD} at intermediate and high inorganic volume fractions. Here in, we demonstrate that E_{BD} can be increased up to these intermediate inorganic volume fractions by creating uniform one-dimensional nanocomposites (nanolaminates) rather than blends of spherical inorganic nanoparticles and polymers. Free standing nanolaminates of highly aligned and dispersed montmorillonite in polyvinyl butyral exhibited enhancements in E_{BD} up to 30 vol % inorganic (70 wt % organically modified montmorillonite). These relative enhancements extend up to five times the inorganic fraction observed for random nanoparticle dispersions, and are anywhere from two to four times greater than observed at comparable volume fraction of nanoparticles. The breakdown characteristics of this model system suggested a trade-off between increased path tortuosity and polymer-deficient structural defects. This implies that an idealized PNC morphology to retard the breakdown cascade perpendicular to the electrodes will occur at intermediate volume fractions and resemble a discotic nematic phase where highly aligned, high-aspect ratio nanometer thick plates are uniformly surrounded by nanoscopic regions of polymer.

KEYWORDS: *dielectric nanocomposite, nanolaminate, layered silicate, permittivity, dielectric breakdown, energy storage*
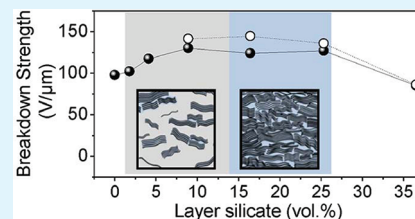
■ INTRODUCTION

Polymer-inorganic nanocomposites (PNCs) are being considered as potential alternatives to polymeric and ceramic dielectrics used for high voltage capacitors, high temperature insulation and gate dielectrics of organic field effect transistors.[1−3] In particular, the potential combination of increased dielectric strength (E_{BD}) and dielectric permittivity (ε_r), along with gradual failure modes, material tunability and processability, provides an attractive alternative over monolithic materials. This is especially important for advanced power systems that require both high energy and power densities, such as pulsed power capacitors. Polymers are currently the preferred material for these extreme applications. For example, manufactured films of biaxially oriented polypropylene (BOPP) exhibit high breakdown fields (E_{BD}) around 600 V/μm, an open circuit failure process, and a maximum energy density (U) of 1−2 J/cm³. Future high power density automotive and aerospace technologies however require substantially greater capacitor performance at a significantly lower space footprint and cost in the form of dielectrics with higher energy density,

greater maximum voltage limits, and scalable uniform defect-free film fabrication.[4−6]

Previous development of dielectric PNCs has generally focused on the introduction of high permittivity (high ε_r) inorganic inclusions to promote an increased effective composite permittivity, while attempting to maintain the underlying polymer breakdown strength (E_{BD}).[7−11] This directly leads to an increase in the theoretically maximum energy storage density, where $U = 1/2\varepsilon_o\varepsilon_r E_{BD}{}^2$. To realize a significant increase in the effective composite permittivity though, effective medium theories, such as the Landauer−Bruggeman approximation for random composite media, necessitate inorganic loadings above 20 vol % because of field exclusion from the high ε_r inorganic phase. Even greater permittivity enhancements may occur at particulate volume fractions above contact percolation, where clusters of the high

dielectric constituent spans the medium between the electrodes, and thus reduces the local field exclusion in the high dielectric consistent.[12−14] As examples along these lines, Kim et al. reported improvements in permittivity, ε_r, to 32, which yielded a theoretical energy density up to 5.6 J/cm^3 for 50 vol % BaTiO$_3$ in P(VDF-HFP).[7] This theoretical maximum energy density is a 15−20% improvement over the of the unfilled P(VDF-HFP). Likewise, Li et al. reported improvements to permittivity, (ε_r = 54) for 30 vol % BaTiO$_3$ nanoparticles in P(VDF-TrFE-CTFE), and measured energy densities at fields substantially below the theoretical breakdown of the pure matrix in the range of 6.9 J/cm^3.[8] In both cases, the increase in effective composite permittivity directly translated into higher energy storage at intermediate fields. However, the presence of spanning clusters, and associated spanning interfaces, provided facile pathways for carrier migration, leading to increased conduction loss and lower breakdown field strength than the pure matrix, thus compromising the maximum potential energy storage ($U = 1/2\varepsilon_o\varepsilon_r E_{BD}^2$). Additionally, field exclusion from the high ε_r component creates a local electrical field in the low ε_r matrix that is greater than the applied field, and enhances the probability of local dielectric failure within the polymer. This intensification of local field, as well as charge migration along interfaces, is enhanced with fractal clustering, and percolation, of the particles.[7,9] Overall, this trade-off between effective permittivity and breakdown field as nanoparticle loading increases confounds efforts to fully maximize the theoretical energy density observed. The question arises, therefore, to what extent can different morphologies and nanoparticle order circumvent this trade-off, and more specifically, what role can nanostructure play in mitigating the processes (initiation and propagation) underlying the dielectric failure event.

The challenge of achieving reproducible nanoparticle dispersion across large length scales, and the coupling between morphology and field enhancement in the matrix, however, confounds the ability to specifically quantify the impact of the morphology on the initiation and subsequent propagation of failure. Commonly, significant agglomeration of the inorganic nanoparticles, and thus fractal clustering, occur because of poor compatibility between the polymer host and inclusion.[9] In essence, the formation (or addition) of inclusions with rough surfaces creates defects, which serve as failure sites. Numerous recent approaches to functionalize the nanoparticle surface have provided avenues to improve compatibility and mitigate severe agglomeration.[7,8,10,11,15−17] Even so, measurable improvements in the maximum breakdown field (E_{BD}) have only been reported in a few rare cases; specifically for polymer nanocomposites with small volume fractions (<3 vol%) of randomly dispersed of inorganic inclusions.[6,15,16,18−21] The resultant nanoparticle morphology, consisting of nanoscopic dielectric heterogeneities and random particle−particle distances, does not appear to behave as critical flaws. Rather, it is thought that the dispersed nanoparticles mitigate the propagation of failure by decreasing charge transport at high operational fields in the form of distributed trap and scattering centers.[15,16,21] Also, a decrease in the probability of free electron avalanche in the polymer phase has been theorized due to reduced bulk charge accumulation and limited electric field enhancement in the polymer phase.[22] For example, Roy and co-workers showed a 20−40% improvement in breakdown strength for silica filled polyethylene.[16] Similar improvements have been shown by Tuncer et.al. for in situ synthesized TiO2 nanoparticles in polyvinyl alcohol and CoFe$_2$O$_4$ nanoparticles

in PMMA.[18,19] Overall, these investigations highlight that PNCs with highly uniform nanoscopic morphology may yield approaches to circumvent the aforementioned trade-off between effective composite permittivity and breakdown field. However, the compositional constraint of low filler loading and relatively low ε_r fillers provide only very marginal gains to the theoretically maximum energy density.

Recent theoretical and experimental investigations indicate that a tailored architecture of oriented and spatially distributed constituents, in the form of high aspect ratio plates or strings can improve the high field response of the composite at loadings greater than observed for dispersed spherical fillers.[20,21,23−25] Vogelsang et al theoretically showed that time to breakdown (voltage endurance) can be prolonged in polymeric insulation with the introduction of multiple overlapping lamellar barriers, of sufficient internal and interfacial strength to direct a breakdown tree along a tortuous route.[24] Analogies between this charge avalanche and gas barrier properties in composites also emphasize that aligned plates may prove to be more effective impediments to transport than random dispersions of spherical particulates.[26] At the macroscale, these lamellar design concepts find parallels in the form of mica laminated insulation. At the mesoscale, Baer et al. recently demonstrated enhanced breakdown strengths for multilayered PVDF/PC films, with layer thicknesses measuring a few tenths of micrometers.[27,28] At the nanoscale, Brandstetter et al.[6] and Imai et al.[21] were the first to experimentally illustrate this concept with low volume fraction of highly aligned organically modified montmorillonite (oMMT) in thermoplastics and thermosets, respectively. Very recently, Tomer et al. confirmed these findings for polyethylene, demonstrating increased E_{BD} for morphologies aligned perpendicular to the field direction.[20] At oMMT fractions <6 wt %, the oriented fillers were thought to frustrate the progression of the electrical tree, whereas the randomly dispersed fillers acted as defect initiators. Overall, nanolamellar concepts should provide a substantially greater number density of barriers relative to microscopic structures. For a given volume fraction of a plates with aspect ratio a, the number density and total surface area will increase proportional to the inverse thickness of the plate. The limitation though is the inability to systematically vary layer spacing and morphology across a large range of compositions, and thus the extent to which these nanolamellar concepts can be exploited to create an extreme density of barriers has not been determined.

Herein, we report on a model system composed of organically modified montmorillonite and polyvinyl butryal where the high degree of compatibility in solution allows control of nanocomposite morphology and filler orientation across the entire range of volume fractions − from pure polymer to pure organically modified montmorillonite. A facile spray processing technique ensures the generation of large area, free-standing, nanolaminate films. These large uniform films enable a statistically relevant assessment of failure, demonstrating that E_{BD} of the nanolaminates can increase 2.5 times relative to the unfilled polymer at 25 vol % inorganic (70 wt % organically modified montmorrillonite). The relatively low dielectric contrast between the organically modified montmorillonite and polyvinyl butryal enables the decoupling of morphology from field enhancement and provides a clearer understanding of the role of morphology on the mitigation of the propagation of failure.

RESULTS AND DISCUSSION

Preparation and Structural Characterization of Nano-laminate Films. Nanolaminate films were prepared by a previously described spray casting technique.[29] Polyvinyl butyral (PVB) and dilmethylditallowammonium modified montmorillonite (oMMT: Cloisite 20A, Southern Clay Products) were premixed in toluene and spray cast to the desired thickness (50−60 μm) onto a fluorinated ethylene propylene (FEP) backing film, attached to a rotary drum using a standard air powered spray gun. The resultant free-standing film, after removal from the FEP and thermal treatment at 125 °C, was flexible, transparent, and sufficiently tough for manual handling during dielectric characterization. Small-angle X-ray diffraction (SAXS) of a 0.81 vol % montmorillonite (2 wt % oMMT)/toluene solution indicated exfoliation of the oMMT with the addition of 0.57 wt % PVB to the solution (see Figures S1 and S2 in the Supporting Information). In brief, low-weight-percent Cloisite 20A (<10 wt %) dispersed in toluene, yielded a viscous, shear thinning, yellow gel that most likely consists of edge−edge and edge−plate association between small (2−10 montmorillonite layers), toluene intercalated tactoids. Similar to prior studies[30−33] utilizing polar organic solvents such as methanol in nonaqueous clay suspensions, the polar silanol and aluminol edge terminal groups ostensibly drive physical gelation. The addition of a small amount of hydrogen bonding additive, such as ethanol or dioxane disrupts this physical association, increasing exfoliation and reducing viscosity, thereby enabling facile processing routes. Gast et al.[30] utilized spectroscopic evidence to suggest the loss of gelation stems from the loss of hydrogen bounding within underlying the physical association of the platelets. Similar effects occur upon addition of PVB to the toluene solution, where the addition of PVB above the optimal concentration decreases solution viscosity, resulting in a stable dispersion of exfoliated oMMT associated with PVB. From these fundamental nanoscale organo-inorganic hybrid building blocks, uniform nanocomposite films can be easily assembled from the "bottom-up" via spray casting and solvent removal.

Figure 1a presents optical images of the spray cast films, demonstrating optical clarity and flexibility. Figure 1b shows the morphology of montmorillonite oMMT-PVB nanocomposite film with 1.3 vol % MMT (5 wt % oMMT). Representative transmission electron micrographs, scanning electron micrographs and associated X-ray diffraction spectra of PVB nanocomposites with increasing MMT content are contained in the Supporting Information (Figures S3−S5). Note that pure oMMT is 43.1 vol % MMT (aluminosilicate layer ∼1 nm; interlayer organic dimethylditallowammonium modifiers ∼2.3 nm). This relatively low inorganic content highlights a geometric trade-off between nanoparticle volume fraction (φ) and spacing (l) that becomes substantial at nanoscopic dimensions. For example, $\varphi \approx (l/t + 1)^{-1}$ for uniformly aligned plates of thickness, t. On the basis of the reasonable assumption that l will not be less than 1−2 nm so as to accommodate surface functionalization, $\varphi_{max} \sim (t/(t + 1))$.

A schematic of the morphology evolution of the nanolaminates with increasing MMT fraction is illustrated in Figure 1c. For the lowest oMMT fractions, TEM confirms the morphology consists of well-dispersed individual MMT layers with a small fraction of clusters comprised of 2−5 coherently stacked layers (tactoids). X-ray diffraction reveals that these small clusters have a basal repeat (d_{001}) of approximately 35.8
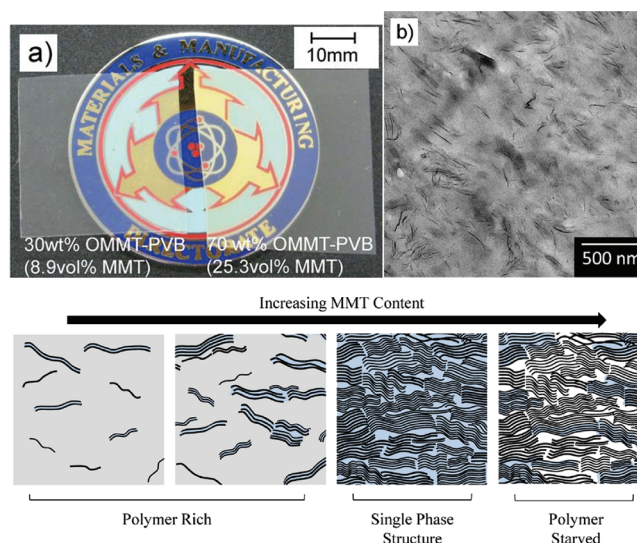

Figure 1. (a) Optical images of 30 wt % oMMT-PVB (8.9 vol % MMT) and 70 wt % oMMT-PVB (25.4 vol % MMT), illustrating film transparency and flexibility across a broad range of inorganic content. Measured film thickness for the 30 wt % oMMT-PVB and 70 wt % oMMT-PVB samples were 55 and 62 μm respectively. (b) Representative micrograph of 5 wt % oMMT-PVB (1.8 vol % MMT) nanolaminate film showing MMT exfoliation. (c) Schematic illustration of the morphology of the oMMT-PVB nanolaminate, as determined from X-ray diffraction and TEM analysis. The MMT layers are denoted by black lines, while matrix PVB is gray and PVB intercalated between the MMT layers is blue. At the highest fraction of inorganic, white signifies regions bereft of polymer. Compositions featured align with 1.8, 16.4, 25.3, and 36.5 vol % MMT.

Å, consistent with the intercalation of PVB between the oMMT layers (d_{001} of unintercalated oMMT is 24.1 Å).[29] Because of the spray casting process, the layers remain well-aligned with the film surface, exhibiting a Herman's orientation parameter (S_d) of 0.52, based on the azimuthal distribution of the d_{001} reflection. At intermediate oMMT content, the fraction of individual MMT layers decrease, and the average number of layers per tactoid increase, as seen in transmission electron microscopy. However, the number density and orientation of uniformly dispersed nanoscopic lamellar units continue to increase. At 25.3 vol % MMT (70 wt % oMMT), the highly aligned tactoids ($S_d = 0.78$) effectively merge and the dominant morphological feature is the intercalated layer spacing of 35.8 Å. This composition is consistent with all the PVB chains occupying the available oMMT interlayer space. As polymer concentration is further reduced, the d_{001} reflection broadens and shifts to smaller spacing, indicating a coexistence of numerous interlayer structures, both intercalated and unintercalated. The films become more fragile, reflecting an increased granular character, arising from physical interactions between tactoids without intervening PVB. This behavior is consistent with prior studies that show the polymer prefers the interlayer regions over the external surfaces of the tactoid.[29] Note that temperature cycling of the 25.3 vol % MMT films, from 20 to 125 °C, held at 125 °C for 24hrs, confirms the stability of the aforementioned morphology. The interlayer spacing reversibly expands and contracts under thermal cycling without any noticeable changes to the macroscopic morphology. These results are consistent with the observed long-term stability of the oMMT-PVB-toluene solution.

1390

dx.doi.org/10.1021/am201650g | ACS Appl. Mater. Interfaces 2012, 4, 1388−1396

Dielectric Characterization of MMT-PVB Nanolaminates. The effective permittivity for the oMMT-PVB nanolaminates, determined at 1kHz, increased from 3.35 for pure polymer to 4.2 for 36.5 vol % MMT (90 wt % oMMT) (see Figure S6 in the Supporting Information). These values for relative dielectric constant across the span of inorganic loading, are in close agreement to the dielectric constants for neat Cloisite 20A, 4.3, and neat PVB, 3.3.[34,35] The low polarization response from the inorganic MMT leads to a small increase effective composite permittivity. Recall that to understand the impact of a nanoscale lamellar morphology on the inhibition of dielectric breakdown, a matrix and inclusion with comparable susceptibility is initially desired so as to minimize the complexity arising from local field exclusion from the high permittivity inorganic phase and associated local field enhancement in the polymer matrix. Overall, the volume fraction dependence of the nanocomposite permittivity is in close agreement to logarithmic and mean field theory.[36,37]

Dielectric breakdown results were analyzed using a 2-parameter Weibull cumulative probability function: $P(E) = 1 - \exp[-(E/E_{BD})^\beta]$, where $P(E)$ represents the cumulative probability of electrical failure, E is the experimental breakdown strength, β is the shape parameter associated with the linear regressive fit of the distribution, and E_{BD} is the cumulative probability of failure at 63.2%, known as the characteristic breakdown strength.[38] Figure 3 summarizes the

Figure 3. Probability of dielectric failure (% probability of sample failure) for the MMT-PVB nanolaminates:. (a) as-fabricated nanolaminates, (b) comparison of between as-fabricated (closed symbols) and consolidated (open symbols) nanolaminate samples.
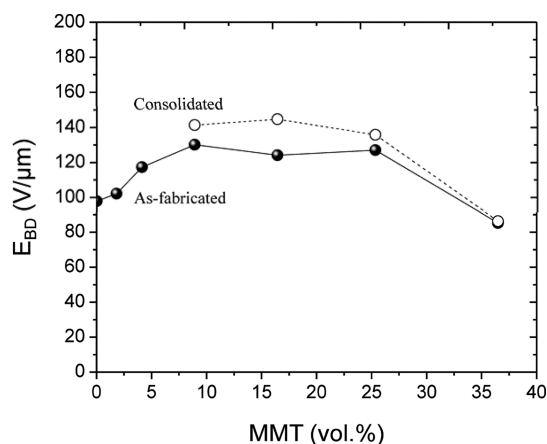

Figure 2. Characteristic breakdown strength (E_{BD}), as a function of MMT volume percent, determined at 63.2% failure probability from a linear regressive fit of the two-parameter Weibull failure analysis.

characteristic breakdown strength (E_{BD}) of as-fabricated and consolidated nanolaminates. The reported values of E_{BD} were extracted from a fit using Weibull failure statistics across 15−20 breakdown tests per MMT volume fraction. Figure 4 summarizes the associated cumulative failure distribution. Note herein that E_{BD} is determined using a parallel plate geometry, and reflects failure associated with the largest flaw existing within the 0.785 cm² sample area. These absolute values of E_{BD} will be lower than those determined by alternative techniques that spatially localize the electric field,[7,9,11,16] and thus neglect issues associated with processing-morphology control. Nevertheless the relative trend of E_{BD} with increasing inorganic loading across the various characterization approaches is illustrative of the impact of morphology on failure, as long as the experiments are referenced relative to a common standard, such as the unfilled matrix.
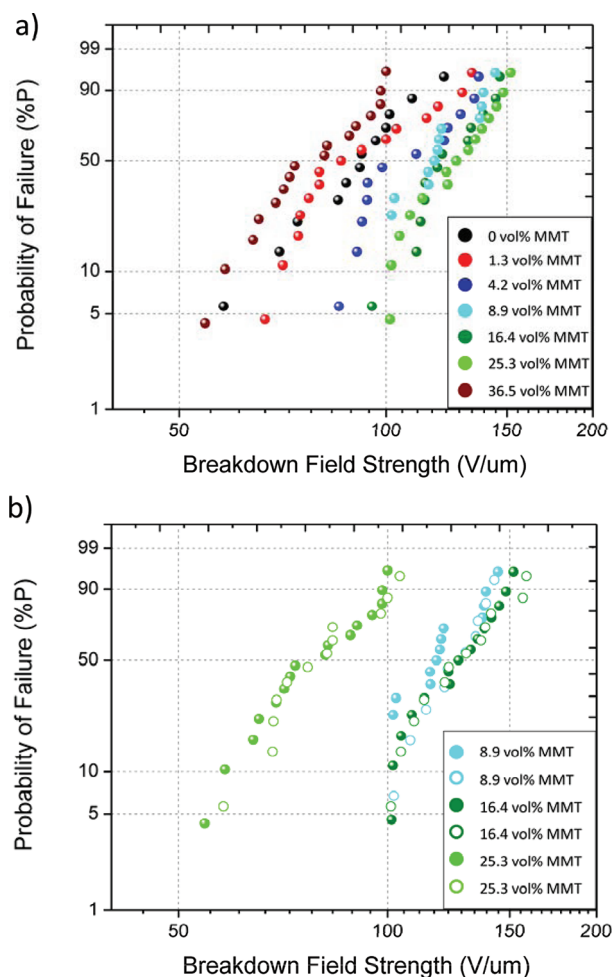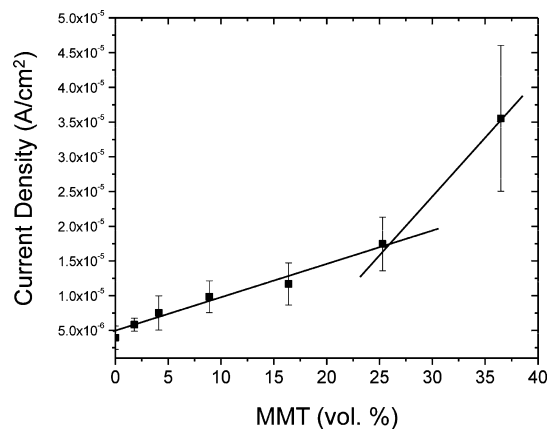

Figure 4. Leakage current density, measured at an applied electric field of 60 V/μm, for PVB-MMT nanolaminates. Error bars represent the standard deviation of 15 samples. Lines provide schematic representation of two trends in current density profile.

The breakdown strength of the MMT-PVB nanolaminates increases up to 16.4 vol % MMT. The maximum breakdown strength occurred between 16.4 and 25.3 vol % MMT, which is approximately a 30% improvement relative to pure PVB. Furthermore, postprocessing consolidation of the nanolaminate

by compression molding of the film at 150 °C and 34.9 MPa, enabled an additional improvement of 20% for the same compositions. These relative enhancements are comparable to prior reports,[6,20,21,39,40] but at four to five times greater inorganic volume fraction. An examination of the cumulative failure distribution for the as-fabricated samples, including neat PVB, shows a bimodal distribution in failure events, which becomes less evident after consolidation (Figure 3b). Consolidation reduces film thickness by approximately 12% for the nanolaminate composition of 25.4 vol % MMT (70 wt % oMMT). No significant change to interlayer spacing, and only slight improvements to layer orientation were observed from XRD (see Figures S4 and S5 in the Supporting Information). Together this implied the reduction of film thickness stems from the elimination of micro voids, which are responsible for premature failure in the as-processed films. It is well-known that plasma formation of air within small voids (0.1−10 μm) drastically reduces breakdown strength. Localized areas containing air voids are expected to breakdown at field strengths between 1 and 3 V/μm.[41]

To understand the trend in breakdown strength of the nanolaminates, first consider the high oMMT content films. At these loadings, the film is effectively a granular consolidate. Although the maximum packing fraction of plates is greater than for spheres, the polydispersity in lateral dimensions of the MMT tactoids implies a maximum packing fraction less than 1. Consequentially, for polymer compositions where the amount of polymer is less than the amount necessitated for full intercalation (herein ~30 wt %), the system harbors a significant fraction of mesoscopic voids located in regions between adjacent tactoids that cannot be eliminated by post processing. As polymer content increases (and MMT content decreases), the additional PVB decreases the concentration of these defects and thus increases breakdown strength.

Next, consider the characteristic breakdown trend from the pure polymer. The addition of a small amount of MMT results in a gradual increase in breakdown strength, which is consistent with the obstruction of localized breakdown events, necessitating a supplementary and tortuous path between and around the inorganic to reach the electrode. As discussed above, this agrees with prior reports of low loadings of well-dispersed layered silicates.[6,20,21,39,40] Using a needle-plate geometry to localize failure events, Imai et al. showed increased dielectric breakdown strength, electrical tree branching and time-to-breakdown with the addition of 1−2 vol % layered silicate to a microsilica/epoxy composite.[21] Brandsetter et.al. reported similar improvements using large area electrodes for a broad range of melt processed thermoplastic − MMT nanocomposite films with 1.3−10 wt % oMMT in linear low density polyethylene (LLDPE), low density polyethylene (LDPE), polyester, and nylon-6.[6]

The enhancements of E_{BD} continue with increasing volume fraction of MMT, and result in a maximum E_{BD} at intermediate MMT loading and prior to a decrease at the highest MMT loading as noted above. Recall, as the MMT content increases, the fraction and size of intercalated inclusions also increase (ie. average number of layers per tactoid increases with oMMT wt %). Also, the orientation of the MMT, with respect to the film surface, increases up to approximately 10 vol %. The simultaneous increase in density, size and orientation of the lamellar inclusions with MMT loading challenges quantitative assessment, as to which is the most important morphological feature relative to increased tortuosity and E_{BD}. Qualitatively though, the scatter parameter (β) in the cumulative probability

distribution improves from 5.54 at 1.3 vol % MMT (5 wt % oMMT) to 8.63 at 16.4 vol % MMT (30 wt % oMMT) (see Table S1 in the Supporting Information). This suggests an evolved insensitivity to defects that precipitate a breakdown event with increased MMT fraction. This insensitivity to macro and mesoscale defects may occur by a narrowing of structural and compositional hierarchy perpendicular to the electrodes. Ideally, minimum structural and compositional hierarchy occurs at the composition of complete interlayer intercalation. This composition corresponds to the lack of free polymer chains outside the volume between MMT layers (25.3 vol % MMT, where PVB intercalated d_{001} = 35.8 Å). Here tactoid separation is minimized and the only morphological length scale is that of the MMT layer (10 Å) and gallery thickness (20−30 Å). Each MMT layer has equal probability to act as an independent barrier to charge propagation.

At intermediate loadings from 16.4 to 25.3 vol% (70 wt % oMMT), the breakdown strength and scatter parameter remain approximately constant. The presence of a plateau strongly suggests competing, antagonistic processes. Morphologically, an intermediate structural feature, such as the tactoid boundaries, rather than individual layers, may determine the scattering probability. This is qualitatively supported by microscopy shown in Figures S3g and S3h in the Supporting Information, where the edges of the MMT layers are correlated, resulting in boundary regions between stacks of intercalated regions and thus, paths of reduced tortuosity. Alternatively (or in addition), an increasing concentration of field-assisted charge carriers associated with the MMT interface may decrease the nanolaminate E_{BD} via internal charge accommodation. Prior impedance studies of commercial oMMT confirmed residual low frequency conductivity arising from excess cationic surfactant (ditallow quaternary ammonium sulfate) and residual salt (NaCl), even after substantially washing and purification as done herein.[34] Low voltage dielectric spectroscopy of the nanolaminates (see Figure S6b in the Supporting Information) though showed minimal ionic influence on dielectric loss, which if present would typically indicate Maxwell−Wagner-Sillars polarization.[42] However, dielectric breakdown occurs at high, not low, electric fields. Figure 4 shows an increased current density at a fixed field (60 V/μm) with increased OMMT content. In general, the leakage current across the oMMT-PVB nanolaminate increases nonlinearly with voltage, reflecting voltage dependent depletion of trapped carriers. Increasing the fraction of oMMT increases the concentration of mobile ionic species at elevated fields, and thus raises charge leakage, as well as reducing the potential energy storage density. Above 25.3 vol % MMT (70 wt % oMMT), the current density increases more rapidly with MMT loading. We speculate that this change in behavior at the fully intercalated concentration reflects the lack of a polymer matrix surrounding the MMT layer edges at the highest MMT loadings. The glassy nature of PVB relative to the void space will reduce charge mobility as well as increase the stability of the hydroxyl groups at the edge of the MMT layers, which are a potential additional source of voltage dependent carriers. In addition to charge accumulation at the electrodes (measured leakage current), free carriers will also accumulate at the internal dielectric boundaries. These ionic processes are dissipative, leading to local heating and a detrimental positive feedback during charge−discharge cycles, where thermal activation of carriers increases with temperature.

Trends in Energy Storage Density. The theoretical energy storage density is related to the characteristic breakdown

strength, E_{BD} (summarized in Figure 2) and ε_r, the dielectric permittivity at 1kHz (see Table S1 in the Supporting Information) via

$$U = \frac{1}{2}\varepsilon_0\varepsilon_r E_{BD}^2 \qquad (1)$$

where ε_0 is the permittivity of free space. In reality, the actual energy storage density is lower because of dissipative processes occurring during charge−discharge cycles, including charge migration and internal depolarization. During use, the maximum energy storage density is also lower, since the maximum system operation voltage will be designed with a safety factor limiting E_{max} to less than E_{BD}. Figure 5 summarizes the theoretical energy storage for the oMMT-PVB system,
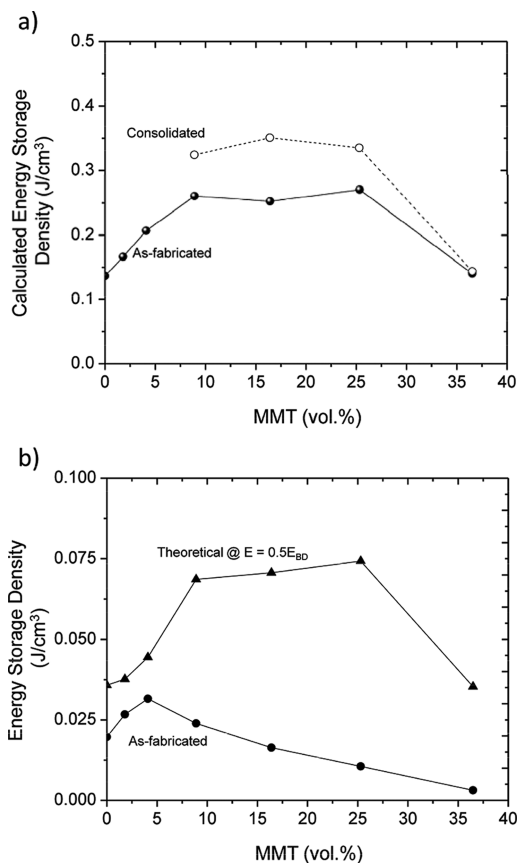

Figure 5. Theoretical and measured energy storage density for MMT-PVB nanolaminates. (a): theoretical energy storage density (eq 1) for as-fabricated (black) and consolidated (red) nanolaminates. (b) Comparison of theoretical energy storage density at $E = 0.5E_{BD}$ and average measured energy density for as-fabricated MMT-PVB nanolaminates (1.8 vol %, 50 V/μm; 8.9 vol % , 65 V/μm; 16.4 vol % , 65 V/ μm; 25.3 vol %, 65 V/μm; 36.5 vol %, 45 V/μm).

calculated from eq 1, as well as the measured recovered energy density at an operation field $E = 0.5E_{BD}$.

The theoretical energy density increases by a factor of 2 with the addition of between 16.4 and 25.3 vol % MMT, Figure 5a. This increase is driven largely through improvements to the breakdown strength arising from the nanolaminate morphology, since permittivity increases only slightly with increased OMMT loading, from 3.2 for neat PVB, to 4.3 for 36.5 vol % MMT (90 wt % oMMT). Furthermore, above 8.9 vol % MMT

(30 wt % oMMT), the layered morphology tolerates the inclusion of defects, in the form of voids present in the as-processed film, which have been shown to severely restrict the application spherical nanoparticles. Post-fabrication consolidation further increases breakdown strength due to elimination of voids and hence, as much as a 2.5× improvement in theoretical energy density is possible.

The trend of theoretical energy density is also observed with measured energy density, as illustrated in Figure 5b. The composition of maximum performance occurs at lower inorganic content, 4.2 vol % MMT (15 wt % oMMT) and gradually decreases for higher MMT volume fractions. The difference between 50% theoretical energy density and that measured at $0.5E_{BD}$ increases with higher inorganic loading, confirming the contribution of the MMT inclusion to the dissipative loss processes within the composite structure. Most likely, this decrease is due to increasing conduction losses and the development of space-charge fields within the nano-composite structure, so even though higher applied fields are possible, more energy is lost because of the resistive nature of the capacitor. Such dissipative processes become increasingly prominent at the highest fields in nanocomposites featuring both high k inorganic inclusions as well as layered silicates.[7,20,27,39] For example, efforts by Tomer et.al. to control the orientation of MMT particulates in polyethylene should higher losses at small fractions MMT (6 wt %), compared to the neat polymer system.[20] Also, extrapolation of their measured energy density at higher applied fields showed a continued divergence between energy density of the neat polymer and nanocomposite. Losses in the filled systems were progressively higher with increasing applied fields. In general, the choice of applied field, and its ratio with E_{BD}, directly impacts the reported values of recoverable energy density. Thus, it is currently difficult to understand structure−performance correlations by comparing the measured energy density values of various systems due to the range of experimental factors.

Finally, for context, Figures 6 provides a comparison of the relative change in the measured breakdown field and the theoretical energy storage density for oMMT-PVB nano-laminate and prior PNC dielectrics. To ensure reasonable comparisons, the literature reports included (1) breakdown statistics for PNCs as well as unfilled matrix; (2) breakdown statistics featuring greater than 10 tests; (3) an extrapolated dielectric constant at 1kHz; and (4) filler loading values expressed in volume fraction. In general, the trends in theoretical energy storage reflected by these selected nano-composite reports are reflective of other reports from the literature. The addition of spherical, high ε_r nanoparticles, such as $BaTiO_3$, result in a steep decline in breakdown strength beginning at low vol% inorganic. The subsequent increase in e_r effectively offsets this decrease and yields a maximum theoretical energy density that is insensitive to filler loading.[7,9,18] Low loadings of dispersed lower ε_r nanoparticles, such as SiO_2, layered silicate or Kaolinite, provide minimal change in effective composite permittivity, but do allow for enhancements to breakdown strength. This combination positively impacts the theoretical energy storage.[16,20,40] The enhanced breakdown behavior of the model MMT-PVB nanolaminate also provides a positive impact to theoretical energy storage; however, the improvements extend to substantially higher volume fractions.
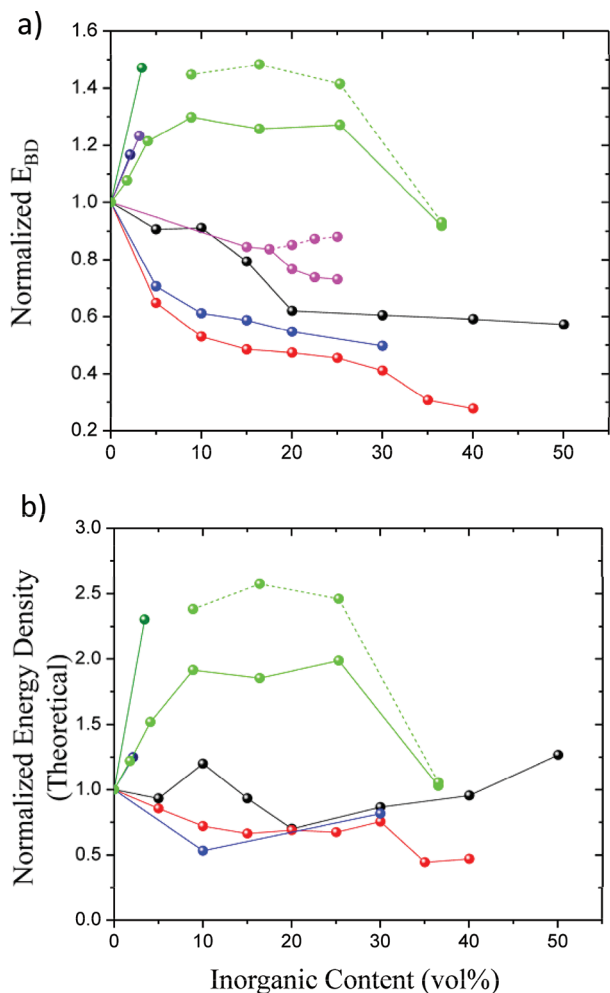
Figure 6. (a) Comparative graphical representation of normalized breakdown field strengths (E_{BD} composite/E_{BD} polymer). (b) Comparative graphical representation of normalized theoretical energy storage ($U_{theoretical}$ composite/$U_{theoretical}$ polymer). MMT-PVB nanolaminate system, as-fabricated (light green, solid line); MMT-PVB nanolaminate system, compressed (light green, dashed line); spherical BaTiO3/poly(vinylidene fluoride-co-hexafluoropropylene) nanoparticle filled nanocomposite (black);[7] spherical BaTiO3/polyimide nanoparticle filled nanocomposite (red);[9] spherical $BaTiO_3$/epoxy nanoparticle filled nanocomposite, random dispersion (pink, solid line);[18] spherical BaTiO3/epoxy nanoparticle filled nanocomposite, x–y aligned (pink, dashed line);[18] spherical SiO2/low-density polyethylene (LDPE) nanoparticle filled nanocomposite, volume fraction estimated using approximations of SiO2 (ρ_{SiO2}, 2.2 g/cm^3) and LDPE (ρ_{LDPE}, 0.91 g/cm^3) densities (navy blue);[16] MMT-LDPE nanocomposite, volume fraction estimated using approximations of MMT (ρ_{MMT}, 1.8 g/cm^3) and LDPE (ρ_{LDPE}, 0.91 g/cm^3) densities (purple);[20] Kaolonite-poly(vinylidene fluoride-co-hexafluoropropylene) nanocomposite, volume fraction estimated using approximations of Kaolinite ($\rho_{Kaolinite}$, 2.63 g/cm^3) and P(VDF-HFP) ($\rho_{P(VDF-HFP)}$, 1.78 g/cm^3) densities (olive green).[38]

■ CONCLUSIONS AND FUTURE OUTLOOK

In summary, the oMMT-PVB model nanolaminate system, which is devoid of field intensification within the matrix phase, provides a foundation to designing architectures from the bottom-up, with the primary goal of staunching electrical breakdown stemming from the matrix phase. The nanolaminate system demonstrates the viability of applying nanoscale plates to form an array of aligned, highly dense interfaces, thereby

providing a significant enhancement to the dielectric breakdown strength, across a large breadth filler volume fractions. This translates into a substantial increase in relative energy storage density, both theoretically and when accounting for dissipative processes present in actual charge–discharge measurements. This intermediate volume fraction behavior has not previously been observed for nanocomposite dielectrics, where morphologies are dominated by spherical fillers and agglomerates at intermediate inorganic loading.

In general, the observed improvement in breakdown strength for the nanolaminates appears to be governed by the density of interwoven, impervious inorganic barriers. This hypothesis has analogies to the current commercially utilized polymeric capacitor, BOPP, which exhibits a polymer morphology of densely packed lamellar crystallites, aligned parallel to the film surface. The significant breakdown strength of BOPP is thought to be derived from the negligible carrier mobility within the crystallites, as well as the packing structure of crystallites that practically eliminates weak regions within the film.[43] In a similar context, the dominant structural feature of the nanolaminate system, intercalated tactoids of MMT, provides a densely packed morphology capable of retarding breakdown and carrier mobility. The impact of the nanoscale layered motif on propagation was also noted by Brandstetter and colleagues who observed a 2–5× increase in the mean time to breakdown for corona endurance tests of various thermoplastic nanocomposites with 1–5 wt % aligned montmorillonite.[6]

Future application of the layered morphology for dielectric nanocomposites remains an open field. Recall that the absolute value of the theoretical energy density of the model oMMT-PVB nanolaminate system is lower than prior reports, where maximum energy density reflected increased permittivity due to high ε_r dielectric fillers and localized testing of E_{BD}.[7–11,13,39] The low e_r of PVB and MMT, as well as the complexity in removing ionic contaminants from the naturally occurring MMT, limits the direct technological adaptation of the oMMT-PVB model system. Future utilization of the morphology motif will need to focus on the creation of nanolaminates from high performance dielectric polymers, such as poly(vinylidene fluoride), and the incorporation of high dielectric inorganic layers. Increasing the absolute composite permittivity, but maintaining low dielectric contrast between matrix and filler, will increase performance beyond prior studies because of the impact of nanolaminate morphology on the propagation of breakdown. Additionally, dispersion of high ε_r nanoplatelets, such as synthetic layered mixed metal phosphonates, BaTi-(O$_3$PC$_6$H$_5$)$_3$ and SrTi(O$_3$PC$_6$H$_5$)$_3$,[44,45] provides an opportunity to investigate the efficiency of the layered approach in controlling breakdown events stemming from field intensification in the matrix phase. Finally, synthetic methods to covalently graft polymers to the nanolayers will provide facile routes to stabilizing the organic/inorganic interface, through molecular trapping and scattering of charged species, as well as fabricate layered morphologies in a manner similar to the spray process utilized in the oMMT-PVB system. Together, these enhancements to the nanolaminate motif could enable a new category of dielectric materials with greater energy storage density for green technologies demanding the rapid delivery of electric power.

■ METHODS

Nanolaminate Film Fabrication. The nanolaminate structures were prepared from Cloisite 20A, a dimethylditallowammounium-

modified montmorillonite (DMDT-MMT, Southern Clay Products) and polyvinyl butyral, (PVB #043, Scientific Polymer). Following established procedures, the DMDT-MMT powder was washed extensively prior to solution blending with the PVB, in order to remove excessive surfactant and ionic impurities resulting from the cation exchange process.[34,46] Washing was accomplished in ethanol, the clay dispersed and stirred for 1 day. The solution was fractionalized in a centrifuge, at 3000 rpm, to remove the solvent, before a second, fresh batch of ethanol was added. The solution was stirred for another day, prior to separation using the centrifuge. A final, third dispersal and centrifuge separation was achieved in ethanol before the washed DMDT-MMT product was added a premixed toluene/PVB solution.

Film fabrication was achieved from solution, utilizing a spray deposition system, outlined previously.[29] After film deposition, the oMMT-PVB films were dried at 125 °C, in a convection oven, to drive off the remaining toluene solvent. Thermogravimetric analysis (TGA), using a Q50 thermogravimetric analyzer (TA Instruments), was used on the fractionated DMDT-MMT/ethanol mix, prior to polymer blending to determine ethanol content as well as after film spray deposition and drying to confirm organoclay content.

The volume fraction of inorganic (montmorillonite) is related to the volume and weight fraction of total OMMT as:

$$V_i^{nc} = V_{om}^{nc} V_i^{om} = \left(\frac{\dfrac{M_{om}^{nc}}{\rho_{om}}}{\dfrac{M_{om}^{nc}}{\rho_{om}} + \dfrac{M_p^{nc}}{\rho_p}} \right) \left(\frac{M_i^{om} \rho_{om}}{\rho_i} \right) \tag{2}$$

where i, om, and p refer to inorganic, oMMT and polymer fractions or densities respectively, while the superscripts om and nc refer to fractions in oMMT and nanocomposite respectively. The fraction of organic content found in Cloisite 20A after washing was determined at 36.7 wt %, from TGA analysis. The densities for oMMT, MMT, and PVB are 1.77, 2.6, and 1.083 g/cm³, respectively. Note the reported densities for layered silicates range from 2 to 3 depending upon organic modifier, specific layered silicate, and manufacturer. The density used for MMT is the average of available experimental and computational values (2.5−2.85 g/cm³, see Table S2 in the Supporting Information).

Nanolaminate Morphology Characterization. Nanolaminate cross-sections, featuring differing content of organo-MMT, were prepared for both scanning electron microscopy (SEM) and transmission electron microscopy (TEM). Film thickness measurements were made using SEM cross sections, prepared utilizing freeze fracturing, prior to vertical mounting, fracture surface upward. Samples were coated with a thin gold layer, using a desktop sputtering system, before being imaged in a Quanta II ESEM (FEI). Transmission electron microscopy was achieved on a 200 kV Phillips CM200 and on a spherical aberration corrected (image corrector) FEI Titan TEM, operating at 300 kV with a GIF Tridiem and low dose system. Cross sections, 70 nm in thickness, were prepared by ultramicrotomy from epoxy embedded nanolaminate films, using a RMC Power Tome and a 35 degree Diatome diamond knife at room temperature.

Wide Angle X-ray diffraction experiments were carried out on a Statton Box camera at varying sample to image plate distances in transmission mode using CuKα, generated from by a Rigaku Ultrax 18 system. Nanolaminate films were cut into 0.1 mm strips, transmission X-ray of the samples was conducted in-plane. 2D image reduction and analysis was carried out using the software package Fit2D,[47] whereas Herman's orientation parameters (S_d) were calculated from the azimuthal distribution of the d_{001} reflection according to previous research by Koerner et al.[48] Basal repeat (d_{001}) was calculated from first and second order peaks of the X-ray diffraction spectra.

Dielectric and Electrical Characterization. Impedance measurements were made on oMMT-PVB nanolaminate films using a Novocontrol Alpha Analyzer accompanied by a Novotherm temperature controller and BDS 1200 sample cell. Between 2 and 3 nanolaminate samples of the same composition, featuring dimensions of 2 cm × 2 cm, were metalized with a 1 cm diameter gold electrode,

on both sides. Electrical contact was achieved with a parallel plate capacitor configuration, using a frequency sweep of 0.1 Hz to 1 MHz, at an AC driving voltage of 1 V. A temperature cycle, featuring incremental heating and cooling between 0−140 °C, at 10 °C steps was used to remove any thermal history and water effects. Phase-sensitive measurements of current and voltage were collected (voltage/current = complex impedance, Z^*) after the final heating/cooling cycle at 20 °C.

Dielectric breakdown measurements were accomplished using a custom-built circuit, featuring a 10 kV Spellman SL300 high voltage supply in a positive N_2 environment. Electrical contact to the nanolaminate films was facilitated using metalized BOPP, as top and bottom electrodes, sandwiching a Kapton mask and the dielectric film, in a configuration commonly used to provide smooth, conformal contact.[49] The Kapton mask featured a circular window with a diameter of 1 cm, providing a contact area of 0.785 cm². A linear voltage ramp of 300 V/s was applied to the sample, with the voltage across the device measured in parallel using a Fluke 289 multimeter, set in peak capture mode. Specimen breakdown was determined from observations of the voltage during the test, as well as visual sparking to the BOPP metalized electrodes. Care was taken to determine the locality of the breakdown event, with respect to the circumference of the Kapton mask. Tests where the breakdown occurred at the edge of the Kapton mask were discarded as atypical of material failure. At the point of breakdown, the HV supply interlock was automatically tripped to isolate the circuit and the peak voltage at breakdown was captured by the multimeter. The BOPP electrodes were discarded after each test, while the Kapton masks was changed after 10 tests to prevent erosion and charred residue from influencing the breakdown behavior. Film thickness in the local region of breakdown was determined using cross-sectional SEM.

Characterization of the leakage current was achieved using a Spellman SR30 HV supply, a HP3549A 4 channel high resistance meter and HP3459A multimeter. The circuit featured computer control through a custom designed Labview program and current/voltage logging during the test procedure. Sample contact was identical to the dielectric breakdown measurements. The voltage was applied to the dielectric film in 100 V increments, followed by a 30 s hold. Steady state current measurements were averaged over the final 2 s of the voltage hold, in order to the remove any effects from the dielectric time constant. Current density was calculated from the steady-state current measurements by dividing by the contact area. Note that the conductivity for pure PVB polymer, measured at an electric field of 60 V/μm, is 7.1×10^{-14} S/cm. oMMT-PVB nanolaminate conductivity at these fields increases by a factor of 3, up to 25.3 vol % MMT .

Energy Density Characterization. Energy storage measurements were made using a charge−discharge circuit. A schematic of the circuit is provided elsewhere.[50] Electrical contact was facilitated using an identical architecture to the breakdown characterization described above. The device under test (DUT) was charged up to predetermined voltage potential using a 10 kV Spellman SL300 high voltage power supply. A manual switch was used to trigger the silicon controlled rectifiers (SCR), discharging the DUT through a high voltage divider, composed of two resistors ($R_1 \gg R_2$). The voltage waveform was captured using a 10× Agilent DSO1012A oscilloscope and the discharged energy storage calculated through the following equation

$$W = \frac{100(R_1 + R_2)}{R_2^2} \int V_0^2 dt \tag{3}$$

■ ASSOCIATED CONTENT

ⓢ Supporting Information

Optical pictures and SAXS data of MMT-toluene-PVB solutions, SAXS spectra of MMT-PVB nanolaminates, SAXS derived MMT interlayer spacing, and SEM and TEM micrographs of MMT-PVB nanolaminates. This material is available free of charge via the Internet at http://pubs.acs.org.

1395

dx.doi.org/10.1021/am201650g | ACS Appl. Mater. Interfaces 2012, 4, 1388−1396

■ AUTHOR INFORMATION

Corresponding Author

*E-mail: Richard.Vaia@wpafb.af.mil.

Notes

The authors declare no competing financial interest.

■ REFERENCES

(1) Cao, Y.; Irwin, P. C.; Younsi, K. *IEEE Trans. Dielectr. Electr. Insul.* **2004**, *11*, 797−807.

(2) Kim, P.; Zhang, X.-H.; Domercq, B.; Jones, S. C.; Hotchkiss, P. J.; Marder, S. R.; Kippelen, B.; Perry, J. W. *Appl. Phys. Lett.* **2008**, *93*, 013302.

(3) Barber, P.; Balasubramanian, S.; Anguchamy, Y.; Gong, S.; Wibowo, A.; Gao, H.; Ploehn, H.; zur Loye, H. C. *Materials* **2009**, *2*, 1697−1733.

(4) Sarjeant, W. J.; Zirnfield, J.; McDougall, F. W. *IEEE Trans. Plasma Sci.* **1998**, *26* (5), 1368−92.

(5) Department of Energy Annual Progress Report for Advanced Power Electronics and Electric Motors, 2010.

(6) Brandstetter, S. S.; Drummy, L. F.; Horwath, J. C.; Schweikart, D. L.; Vaia, R. A. *IEEE Trans. Dielectr. Electr. Insul.* **2008**, *15*, 287−290.

(7) Kim, P.; Doss, M. N.; Tillotson, J. P.; Hotchkiss, P. J.; Pan, M-J; Marder, S. R.; Li, J.; Calame, J. P.; Perry, J. W. *ACS Nano* **2009**, *3*, 2581−92.

(8) Li, J.; Soek, S. I.; Chu, B.; Dogan, F.; Zhang, Q.; Wang, Q. *Adv. Mater.* **2009**, *21*, 217−21.

(9) Dang, Z.-M.; Lin, Y.-Q.; Shi, C.-Y.; Li, S.-T.; Bai, J. *Adv. Funct. Mater.* **2008**, *18*, 1509−1517.

(10) Li, J.; Claude, J.; Norena-Franco, L. E.; Seok, S. I.; Wang, Q. *Chem. Mater.* **2008**, *20*, 6304−06.

(11) Jung, H. M.; Kang, J.-H.; Yang, S. Y.; Won, J. C.; Kim, Y. S. *Chem. Mater.* **2010**, *22*, 450−456.

(12) Calame, J. P. *J. Appl. Phys.* **2006**, *99*, 084101.

(13) An, L.; Boggs, S. A.; Calame, J. P. *IEEE Electr. Insul. Mag. (USA)* **2006**, *24*, 5−10.

(14) Li, J. Y.; Zhang, L.; Ducharme, S. *Appl. Phys. Lett.* **2007**, *90*, 132901.

(15) Ma, D.; Siegel, R. W.; Hong, J-I; Schadler, L. S.; Martensson, E.; Onneby, C. *J. Mat. Sci.* **2004**, *19*, 857−64.

(16) Roy, M.; Nelson, J. K.; MacCrone, R. K.; Schadler, L. S. *J. Mat. Sci.* **2007**, *42*, 3789−99.

(17) Tchoul, M. N.; Fillery, S. P.; Koerner, H.; Drummy, L. F.; Oyerokun, F. T.; Mirau, P. A.; Durstock, M. F.; Vaia, R. A. *Chem. Mater.* **2010**, *22*, 1749−59.

(18) Tuncer, E.; Sauers, I.; James, D. R.; Ellis, A. R.; Paranthaman, M. P.; Goyal, A.; More, K. L. *Nanotechnology* **2007**, *18*, 325704.

(19) Tuncer, E.; Rondinone, A. J.; Woodward, J.; Sausers, I.; James, D. R.; Ellis, A. R. *Appl. Phys. A: Mater. Sci. Process.* **2009**, *94*, 843−52.

(20) Tomer, V.; Polizos, G.; Randall, C. A.; Manias, E. *J. Appl. Phys.* **2011**, *109*, 074113.

(21) Imai, T.; Sawa, F.; Nakano, T.; Ozaki, T.; Shimizu, T.; Kozako, M.; Tanaka, T. *IEEE Trans. Dielectr. Electr. Insul.* **2006**, *13* (1), 319−26.

(22) Lewis, T. J. *IEEE Trans. Dielectr. Electr. Insul.* **2004**, *11*, 739−53.

(23) Danikas, M. G.; Tanaka, T. *IEEE Electr. Insul. Mag. (USA)* **2006**, *25* (4), 19−25.

(24) Vogelsang, R.; Farr, T.; Frohlich, K. *IEEE Trans. Dielectr. Electr. Insul.* **2006**, *13* (1), 373−82.

(25) Tomer, V.; Randall, C. A. *J. Appl. Phys.* **2008**, *104*, 074106.

(26) Gusev, A. A.; Lusti, H. R. *Adv. Mater.* **2001**, *13* (21), 1641−1643.

(27) Wojak, M. A.; Pan, M.-J.; Wan, A.; Shirk, J. S.; Mackey, M.; Hiltner, A.; Baer, E.; Flandin, L. *Appl. Phys. Lett.* **2008**, *92*, 113301.

(28) Mackey, M.; Hiltner, A.; Baer, E.; Flandin, L.; Wolak, M. A.; Shirk, J. S. *J. Appl. Phys D.* **2009**, *42*, 1−12.

(29) Dunkerley, E.; Koerner, H.; Vaia, R. A.; Schmidt, D. *Polymer* **2011**, *52* (4), 1163−71.

(30) Gast, R. G.; Motrland, M. M. *J. Colloid Interface Sci.* **1971**, *37*, 80−92.

(31) Iwasaki, T.; Onodera, Y.; Torii, K. *Clays Clay Miner.* **1989**, *37* (3), 248−57.

(32) Dekany, I.; Szanto, F.; Weiss, A.; Lagaly, G. *Ber. Bunsen-Ges. Phys. Chem.* **1986**, *90* (5), 427−431.

(33) Slabaugh, W. H.; Hanson, D. B. *J. Colloid Interface Sci.* **1969**, *29*, 460−463.

(34) Jacobs, J. D.; Koerner, H.; Heinz, H.; Farmer, B. L.; Mirau, P.; Garrett, P. H.; Vaia, R. A. *J. Phys. Chem. B* **2006**, *110* (41), 20243−157.

(35) Mehendru, P. C.; Kumar, N.; Arora, V. P.; Gupta, N. P. *J. Chem. Phys.* **1982**, *77*, 4232.

(36) Landau, L. D., Lifshitz, E. M., *Electrodynamics of Continuous Media*, 2nd ed.; Pergamon Press: Oxford, U.K., 1984.

(37) Lichtenecker, K. *Phys. Zeit.* **1926**, *27*, 115−158.

(38) Weibull, W. *J. Appl. Mech.* **1951**, *18*, 293−297.

(39) Tomer, V.; Polizos, G.; Manias, E.; Randall, C. A. *J. Appl. Phys.* **2010**, *108*, 074116.

(40) Tomer, V.; Manias, E.; Randall, C. A. *J. Appl. Phys.* **2011**, *110*, 044107.

(41) Dissado, L. A., Fothergill, J. C. *Electrical Degradation and Breakdown in Polymers*; Peter Peregrinus; London, 1992.

(42) Sillars, R. W. *J. Inst. Electr. Eng.* **1937**, *80*, 378−394.

(43) Gao, L. Y.; Tu, D. M.; Zhou, S. C.; Zhang, Z. L. *IEEE Trans. Electr. Insul.* **1990**, *25* (3), 535−40.

(44) Barber, P.; Houghton, H.; Balasubramanian, S.; Anguchamy, Y. K.; Ploehn, H. J.; zur Loye, H.-C. *Chem. Mater.* **2009**, *21* (7), 1303−10.

(45) Barber, P.; Pellechia, P. J.; Ploehn, H. J.; zur Loye, H.-C. *ACS Appl. Mat. Interfaces* **2010**, *2* (9), 2553−59.

(46) Schmidt D. F. *Polysiloxane/Layered Silicate in Nanocomposites: Synthesis, Characterization and Properties*. PhD Thesis, Cornell University, Ithaca, NY, 2003

(47) Hammersley, A. P.; Svensson, S. O.; Hanfland, M.; Fitch, A. N.; Haeusermann, D. *High Press. Res.* **1996**, *14*, 235−48.

(48) Koerner, H.; Luo, Y.; Li, X.; Cohen, C.; Hedden, R. C.; Ober, C. K. *Macromolecules* **2003**, *36*, 1975−81.

(49) Ho, J.; Ramprasad, R.; Boggs, S. *IEEE Trans. Dielectr. Elect. Insul.* **2007**, *14* (5), 1295−1301.

(50) Shu, E. W.; Klimas, J.; Boggs, S. A. *IEEE Trans. Dielectr. Insul.* **2010**, *17*, 10−20.